Available online at www.sciencedirect.com
ScienceDirect
Journal of the European Ceramic Society 31 (2011) 1779–1789
www.elsevier.com/locate/jeurceramsoc

# Influence of nano-aluminum filler on the microstructure of SiOC ceramics

Liviu Toma *, Claudia Fasel, Stefan Lauterbach, Hans-Joachim Kleebe, Ralf Riedel

*Fachbereich Material- und Geowissenschaften, Disperse Feststoffe, Technische Universität Darmstadt, 64287 Darmstadt, Germany*

Received 28 October 2010; received in revised form 15 February 2011; accepted 7 March 2011
Available online 1 April 2011

**Abstract**

Ceramic SiC–mullite–$Al_2O_3$ based nanocomposites were successfully obtained at temperatures below 1500 °C after pyrolysis and annealing of green compacts prepared by cross-linking and shaping in a warm press step of commercial poly(methylsilsesquioxane) MK polymer mechanically mixed with aluminum filler having nanoparticle size. The heat treatment takes place under the exclusion of oxygen (inert argon atmosphere) and temperatures as low as 800 °C initiate the crystallization of a silicon carbide phase. The influence of the nano-aluminum filler and of the pyrolysis temperature on the crystallization behavior of the materials has been investigated. It was confirmed that an appropriate amount of nano-aluminum filler leads to a cristobalite free bulk SiOC ceramic. In consequence, the received ceramic samples have to be considered as a nano/micro-ceramic composite consisting of crystals of mullite (average dimension in the range of 200 nm), silicon carbide (20 nm) and α-alumina (50 nm).


*Keywords:* Nanocomposites; Mullite; $Al_2O_3$; SiC

## 1. Introduction

Ceramic matrix nanocomposites are of considerable technological interest due to their combined thermal and mechanical properties such as low-temperature densification, machinability, and superplastic behavior.[1–4] The improvement of diverse physical properties can be achieved nowadays following a common strategy: to design the microstructure of the advanced ceramic at a nanoscale level by the fabrication of composites. Therefore, well established and reliable processing routes are required to control the microstructure and the properties of ceramic nanocomposites. Bulk nanocomposites can be generally fabricated by conventional powder processing, sol–gel and polymer pyrolysis techniques. Technical difficulties in the conventional processing methods, namely the powder processing and sol–gel processing routes, hinder the wider use of such structural ceramic nanocomposites. These difficulties are mainly related with microstructural control due to inhomogeneous dispersion of the phases in the matrix having detrimental effects on densification and mechanical properties. An alternative method of preparing ceramic nanocomposites is the active-filler controlled pyrolysis method originally developed by Greil[5–8] as a single step fabrication route to obtain zero shrinkage polymer-derived ceramics for complex three-dimensional components. Polysilsesquieoxanes resins, with the general chemical formula $[RSiO_{1,5}]_n$, can be cross-linked by polycondensation or polyaddition reactions with the help of a catalyst into duroplastic materials at elevated temperatures. Further pyrolytic conversion leads to a SiOC glass associated with a significant shrinkage of the fabricated bodies. In order to reduce the shrinkage, inorganic filler materials (active and passive) were used to influence the thermolysis process. Active fillers such as metallic or intermetallic compounds react mainly with the gaseous products generated during the polymer-to-ceramic conversion, but also with the heating of gas and/or the ceramic residue, generating carbides, nitrides, oxides, or silicides. In the case of passive fillers, no reaction occurs between the filler and the matrix or the decomposition products. The main advantages of the polymer-to-ceramic transformation process are the low processing temperatures and the possibility of using polymer forming techniques to obtain complex shapes.[6,8–10]

The influence of aluminum filler with a particle size range between 50 and 80 nm in polymethylsiloxane (PMS MK polymer) on the ceramization process (pyrolysis), crystallization behavior and microstructural development of the polymer-derived SiAlOC ceramics obtained after different heat treatment temperatures was studied in the present work. A key question was to understand the transformation of the filled preceramic

* Corresponding author. Tel.: +49 6151 16 6342; fax: +49 6151 16 6346.
*E-mail address:* toma@materials.tu-darmstadt.de (L. Toma).

0955-2219/$ – see front matter © 2011 Elsevier Ltd. All rights reserved.
doi:10.1016/j.jeurceramsoc.2011.03.011

polymer to the nanostructured ceramic and the role of the active filler in the ceramization process and on the ceramic microstructure. A secondary purpose of this work was to create a nanocomposite material in the pseudo ternary system SiC–mullite–$Al_2O_3$ because it has been shown that SiC–mullite, SiC–$Al_2O_3$, and mullite–SiC systems have excellent mechanical properties.[4,11–16] Carefully choosing the experimental/synthetic conditions and using aluminum nanoparticles, we try to keep the size of the crystalline phases after annealing in the nanometric range and to suppress the formation of objectionable cristobalite phase. However, the aim of the study was solely focused on the reaction phenomena associated with the pyrolysis process and on the structural and microstructural characterization of the SiAlOC ceramics.

The polymer-to-ceramic transformation of the polysiloxane MK polymer performed under argon atmosphere below 1300 °C yields an amorphous SiOC matrix; above this temperature the segregation of a SiC phase is observed. The influence of aluminum as a filler on the MK polymer and other polysiloxanes was investigated intensely in oxidizing conditions by the pyrolysis in air. The goal of such studies was to produce dense mullite ceramics at relatively low temperatures.[17–20] Detailed studies of the evolution of phases during the pyrolysis are also presented in the above mentioned literature and show that the thermal decomposition of the polymers in the presence of aluminum in air proceeds by a complex series of reactions which shows elemental Si, SiC and α-$Al_2O_3$ as intermediates. Moreover, the size and morphology of the starting Al powder controls the pyrolysis reaction pathway and kinetics.[17–20] The first data on the pyrolysis under inert atmosphere of an aluminum filled polysiloxane indicate the formation of a SiC–$Al_2O_3$ phase at temperatures as high as 1200 °C.[21] Recently, following a polymer gel approach using a cross-linking agent on concentrated polymethylsilsesquioxane resin solutions, the influence of aluminum micro and nano particles during pyrolysis under inert atmosphere was also investigated showing the formation of mullite, alumina, silicon carbide and cristobalite phases in the resulting ceramics.[22] Interestingly, the formation of free silicon and $Al_4C_3$ as intermediate phases during ceramization was found in that work. However, detailed investigations of the ceramization process as well as of the ceramic microstructure of polymer-derived SiOC ceramics synthesized in the presence of nano-Al fillers have not been reported in the literature so far.

The influence of aluminum on the polysiloxane MK polymer during pyrolysis was studied with the aid of different investigation methods like thermogravimetric analysis (TGA), differential thermal analysis (DTA), and in situ evolved gas analysis using mass spectrometry (MS). In addition, ex situ methods like X-ray diffraction (XRD) in combination with Rietveld refinement, micro-Raman spectroscopy, and electron microscopy (SEM and TEM) were used to obtain morphological and structural information.

## 2. Experimental procedure

A solid thermosetting commercial poly(methylsilsesquioxane) (Wacker-Belsil$^{TM}$ PMS MK®, solid silicone resin, solvent free, described by the following basic composition: $(CH_3–SiO_{3/2})_x$) was used as the starting preceramic polymer. The polymer possesses approximately 2 mol% hydroxyl- and ethoxyl-groups as functional units, and with evolution of water and ethanol by polycondensation reaction, the formation of a three dimensional network with Si–O–Si alternating units as the backbone takes place. Zirconium acetylacetonate ($C_{20}H_{28}O_8Zr$, Sigma–Aldrich, USA, referred to as catalyst) was used as a cross-linking agent.[23]

Aluminum (50–80 nm particle size, H.C. Starck, Germany) was used as a filler. The mixture AlMK (11 vol.% aluminum + 89 vol.% MK polymer) was prepared in a planetary ball mill, sieved (100 μm), cross-linked during warm pressing (180 °C, 25 MPa, 30 min) using a hydraulic press (warm press type 123, H. Collin) and subsequently pyrolyzed for 3 h under flowing argon atmosphere at temperatures of 1100, 1200, and 1300 °C. Further annealing treatments (argon atmosphere, 1400 °C and 1500 °C for 3 h) were performed on bulks pyrolyzed at 1300 °C in argon atmosphere to analyze the crystallization behavior.

Simultaneous thermal analysis (TG/DTA) using a Netzsch STA 449C Jupiter operating in argon flow (25 ml/min) with a heating rate of 5 °C/min up to the maximum temperature of about 1400 °C was used to study the pyrolytic transformation from polymer to ceramic of the green bodies. Analyses of the evolved gases were obtained in situ by a coupled quadrupole mass spectrometer (QMS 403C Aëolos). The carbon content of the powdered ceramic samples was determined with a carbon analyzer (Leco, Type C-200), and the oxygen content with a N/O analyzer (Leco, Type TC-436). Chemical analysis of Al was performed at the Mikroanalytisches Labor Pascher (Remagen/Germany), while the silicon content was the difference calculated from 100%. Micro-Raman spectra were recorded on a Horiba HR800 micro-Raman spectrometer using an excitation laser wavelength of 514 nm. A Varian FT-IR spectrometer (model 670, resolution 4 $cm^{-1}$ Varian Deutschland GmbH), was used to record the FT-IR spectra of the samples (in the KBr pellet) in the range of 400–4000 $cm^{-1}$.

Powdered samples were investigated by X-ray diffraction analyses (diffractometer model STADI P in transmission/Debye–Scherrer geometry with linear PSD, STOE, Darmstadt, Germany, using a curved Ge (1 1 1) monochromator and Cu $K_\alpha$ radiation). The quantitative determination of SiC, mullite and α-$Al_2O_3$ in the ceramic samples was obtained from X-ray diffraction data by using Rietveld refinement performed with Fullprof, available in the software package Winplotr.[24] The structural parameters and atomic positions for SiC, mullite and α-$Al_2O_3$ were taken from the literature.[25–27]

For measuring the skeletal density of the compacts the Archimedes method was applied using distilled water as an immersion liquid (samples were boiled in water before the measurements). The bulk density was calculated by the ratio mass over volume and the open porosity was determined by the ratio bulk/skeletal density. Resulting phase composition and microstructure of the ceramic materials were investigated by scanning electron microscopy (SEM) (JEOL 6300F SEM microscope at 5 kV), and transmission electron microscopy (TEM)

(FEI CM20STEM, Eindhoven, The Netherlands, operating at 200 kV, $LaB_6$ cathode). TEM samples were prepared using standard ceramographic techniques, which included grinding, dimpling, and ion milling, followed by coating the sample with a thin carbon layer to avoid charging of the sample in the TEM.

## 3. Results and discussions

The green body bulk sample AlMK was analyzed by simultaneous thermal analysis coupled with in situ mass spectrometry (MS) (Fig. 1). Before describing the ceramization process of the aluminum filled MK polymer with the above mentioned experimental method, we will first summarize briefly the observations gained in the case of pure MK polymer for assessment reasons. The available studies reported in the literature[28,29] show that the polymer-to-ceramic transformation of the polysiloxane MK polymer occurs in three steps and shows a ceramic yield of 86 wt.%. The first weight loss step is due to polycondensation during the cross-linking process and results in the release of $H_2O$, ethanol, n-propanol and octamethyl T8 polyhedral oligosilsesquioxane (POSS). The further two mass loss steps correspond to the starting and ending of the ceramization process. The evolution of the POSS octamethyl T8 group is the result of the cross-linking step and may appear during the decomposition of the polysiloxane backbone of non-cross-linked oligomers.[29] Hydrogen, methane and small amounts of water are detected by in situ IR spectroscopy and MS.[28,29]

In the case of the aluminum filled AlMK sample, Fig. 1a shows the TGA, DTG (first derivative of TG) and DTA curves, the specific mass loss during pyrolysis is found to be 8 wt.%. The cross-linking process occurs over a wide temperature range and strings together three mass loss steps (from 95 to 250 °C, DTG peak at 145 °C; from 250 to 500 °C, DTG peak at 349 °C, from 500 to 590 °C, DTG peak at 531 °C). In these temperature ranges the masses $m/z = 15$, 27 and 29 refer to ethyl fragments, as well as to the main mass fragments of acetaldehyde, corresponding to a decomposition of the included solvent acetone[23] (Fig. 1b). The evolution of water, methanol and ethanol was not observed by in situ mass spectrometry up to 600 °C. The cross-linking process in the temperature regime ranging from 400 to 660 °C is accompanied by the reaction of solid Al with the oxygen rich Si–O–C matrix to form alumina.[30] The ceramization process takes place in two mass loss steps (from 600 to 725 °C, DTG peak at 680 °C, and from 725 to 900 °C, DTG peak at 747 °C) and the MS reveals the evolution of water ($m/z = 17$, 18, Fig. 1c) and $CO_2$ ($m/z = 12$ and $m/z = 44$, Fig. 1d). Evolution of $CO_2$ and water is also analyzed in the case of pure MK polymer and might be attributed to the oxidation of the methyl group by the oxygen rich matrix.[31]

The differential thermal analysis (DTA) curve analysis reveals two weak exothermic peaks at 680 and 795 °C respectively. The position of the first peak is only 20 °C higher than the melting point for Al and is in good agreement with the DTG peak of the first mass loss step of the ceramization process, as well as with the maximum of the MS spectra observed for water and $CO_2$ species release (see Fig. 1c and d). This finding is consistent with the fact that during melting and above the melting temperature of aluminum ($T_m = 660$ °C) the oxidation of Al is accelerated as shown also by the second exothermic peak at 795 °C. Due to the thermal expansion of the melt the rupture of the oxide scale results in a rapid oxidation of Al in the liquid state into $Al_2O_3$.[30] Modification of MK polymer with Al filler considerably changes the cross-linking behavior in comparison with the Al-free MK polymer; the ceramization process is clearly affected by the oxidation of Al inside the preceramic matrix.

The phase evolution for the AlMK system between 600 and 1500 °C as determined by X-ray analysis is shown in Fig. 2. The crystalline phases present in the AlMK sample at 600 °C are aluminum, silicon and aluminum carbide. The reaction product has been confirmed as rhombohedral aluminum carbide of the type $A1_4C_3$.[32] Thus, the presence of silicon and aluminum carbide clearly shows that a chemical reaction between aluminum and the amorphous silicon oxycarbide matrix takes place during the ceramization process. The reaction result implies that Al readily reacts with free carbon and/or hydrocarbons which are parts of the Si(O,C) matrix or forming during the ceramization process, as is the case for methane detected in pure MK polymer but not in the AlMK system forming $Al_4C_3$ even before Al melts, suggesting that carbon is in close contact with aluminum.[33] The formation of the silicon in the matrix can also be explained by the oxygen consumption caused by a reaction of the Si(O,C) matrix with aluminum. At 600 °C the XRD pattern exhibits no traces of the expected γ-$Al_2O_3$ phase. This is consistent with the conclusion that the reaction products of oxidized Al powder are mainly amorphous $Al_2O_3$.[30] These findings result in the conclusion that the SiOC matrix may react with Al following the reaction (1) below, as suggested also in early studies on fiber-reinforced aluminum alloy composites[34]:

$$3SiOC + 6Al \rightarrow Al_2O_3 + Al_4C_3 + 3Si \quad (1)$$

Increasing the pyrolysis temperature to 700 °C resulted in a severely reduced content of metallic aluminum, compared to the result at 600 °C. Significant quantities of crystalline Si and $Al_4C_3$, as well as a small amount of γ-$Al_2O_3$ phase were found by XRD in the sample pyrolyzed at 800 °C. Surprisingly, even at this temperature the crystallization of β-SiC can be observed ({1 1 1} diffraction peak of the cubic SiC polymorph at $2\theta = 35.7°$, and the related {1 0 1}, {2 1 1} reflections at $2\theta = 60°$, 72°, respectively). The increase of the pyrolysis temperature promotes even more the segregation of the silicon carbide phase which is clearly detected up to 1500 °C. A direct reaction between liquid Al and SiC can also occur during the ceramization forming $Al_4C_3$ and metal Si according to the reaction (2)[35–38]:

$$4Al + 3SiC \rightarrow Al_4C_3 + 3Si \quad (2)$$

For the free-energy change of the reaction to be negative, silicon produced by the reaction must dissolve in the liquid aluminum in order to reduce its activity.[38] The aluminum carbide is a brittle reaction product that lines the filler–matrix interface, and silicon, the other reaction product, dissolves in aluminum, lowering its melting temperature.[36,37] X-ray diffraction lines of Si

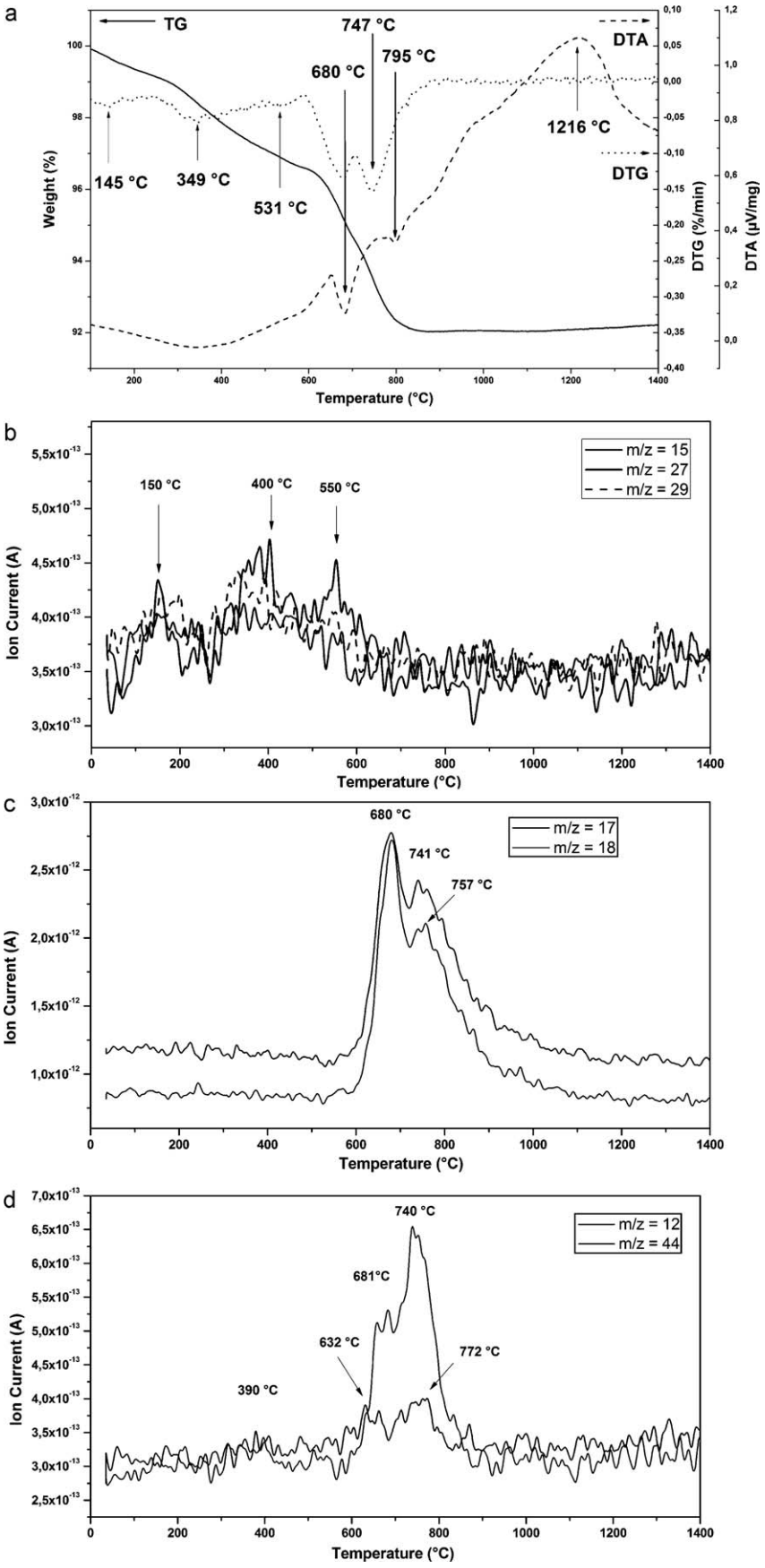


Fig. 1. Thermal analysis of AlMK sample: (a) TG with its first derivative plot (DTG) and DTA curve; in situ mass spectroscopy with (b) methane evolution and acetone decomposition $m/z = 15$, $m/z = 27$ and $m/z = 29$, (c) water evaporation $m/z = 17$, $m/z = 18$, and (d) $CO_2$ release $m/z = 12$ and $m/z = 44$.

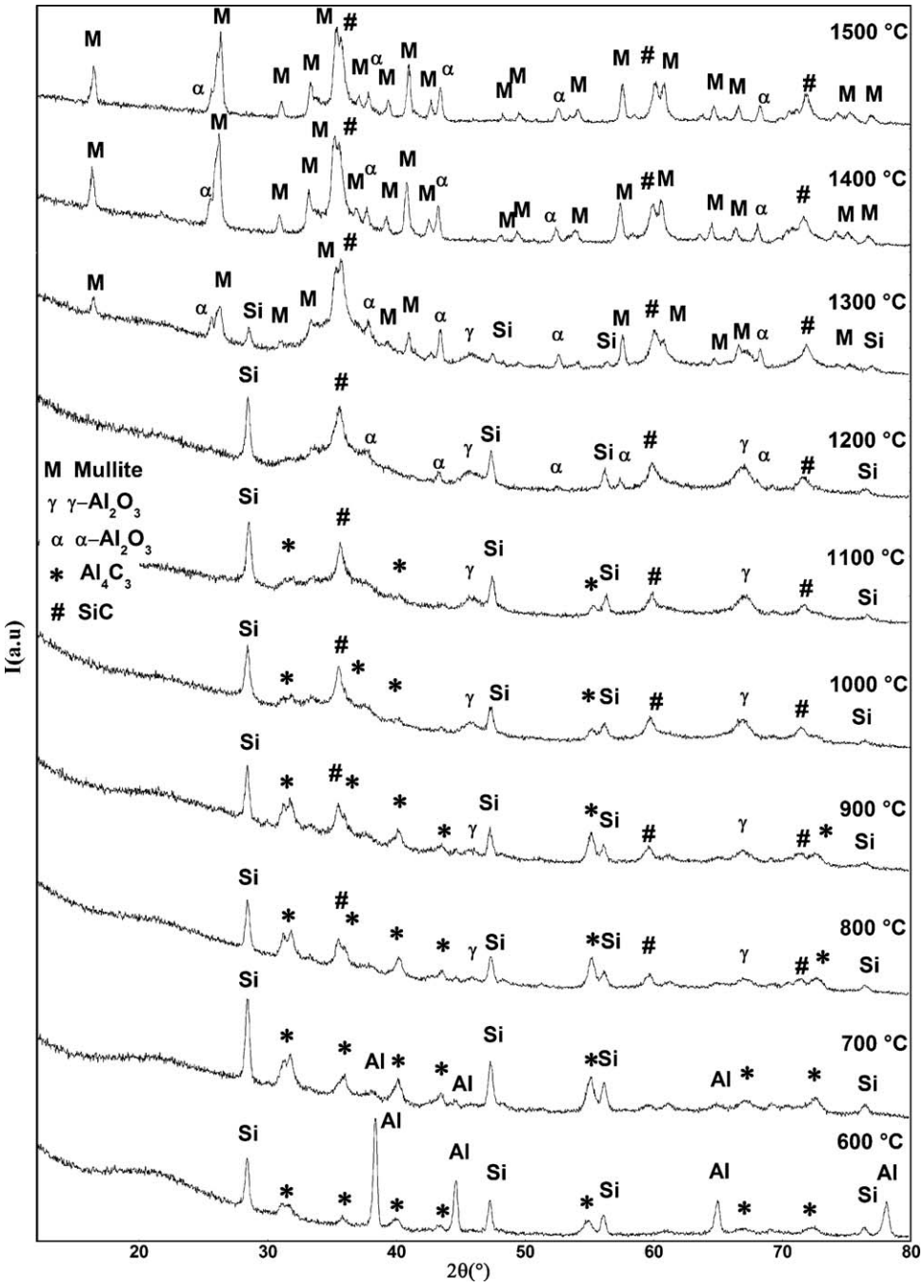


Fig. 2. X-ray diffraction analyses of the obtained ceramics for the samples AlMK.

are detectable up to 1300 °C, while for the $Al_4C_3$ phase 1100 °C was the highest temperature at which this phase was observed in XRD. Further transformation of the aluminum into alumina increases the amount of dissolved silicon in the liquid aluminum and the reaction tends to saturate. At this point the opposite reaction starts and the aluminum carbide phase is consumed. In consequence, we find an increase in the amount of the silicon carbide phase in the ceramic matrix as well as that of the alumina phase.

Crystalline silicon as well as γ-$Al_2O_3$ can be detected in the samples heat-treated up to 1300 °C. The γ-$Al_2O_3$-to-α-$Al_2O_3$ phase transformation usually takes place at around 1100 °C but in the presence of amorphous $SiO_2$ the transition temperature can rise up to 1300 °C.[23,39] Although it is expected that the δ- and θ-$Al_2O_3$ transition phases are also present in the ceramic matrix, their X-ray reflexes were not found in the XRD patterns. The reflexes of α-$Al_2O_3$ phase are detected starting with 1200 °C, and at 1300 °C mullite starts to form. The mullite coexists with α-$Al_2O_3$ and silicon carbide from 1300 up to 1500 °C. From 600 to 1300 °C all samples are characterized by a relatively high background which shows that the ceramic matrix also contains an amorphous phase as indicated by the presence of a silica halo centered at about $2\theta = 22°$. By increasing the annealing temperature up to 1400 and 1500 °C the silica halo completely disappears.

Table 1
Crystallite size dimensions calculated by Debye–Scherrer equation (nm).

| Sample | AlMK | |
|---|---|---|
| Annealing temperature | 1400 °C | 1500 °C |
| Mullite | 50 | 60 |
| SiC | 5 | 7 |
| α-Alumina | 42 | 42 |

Table 2
Results for the quantitative analyses (wt.%) and details of the Rietveld refinement.

| Sample | AlMK | |
|---|---|---|
| Annealing time | 1400 °C | 1500 °C |
| Mullite | 42.8 | 46.1 |
| SiC | 41.6 | 33.6 |
| α-Alumina | 15.6 | 20.3 |
| $R_p$ (%) | 7.38 | 9.17 |
| $R_{wp}$ (%) | 10.2 | 12.8 |
| $R_{wp}$ (expected) (%) | 6.44 | 8.48 |
| $\chi^2$ | 2.52 | 2.28 |

The crystallite sizes of mullite, silicon carbide and alumina phases were estimated with the aid of Scherrer equation[40] and are presented in Table 1. Instrumental contributions to peak broadening were determined using Si as a standard reference material and were taken into consideration during the analysis.[41] The crystallite size of the mullite phase remains unchanged during the heat treatment (1400 and 1500 °C) with values close to 60 nm. The crystallite size for the silicon carbide is smaller, with a value smaller than 10 nm. The size of the α-alumina is found to be in the range of 40 nm.

Enhanced formation of the silicon carbide phase is noted at temperatures above 800 °C; the XRD patterns show that the β-SiC phase is incorporated into the ceramic matrix. However, the XRD pattern deviates from the ideal 3C pattern showing a significant enhancement of the background around the basic peak at $2\theta = 35.7°$, and an extra peak at $2\theta = 33.7°$, clearly seen in the case of the AlMK sample annealed at 1500 °C. These additional features indicate a multitude of planar defects (stacking faults and microtwins) present in the β-SiC phase[42–45]; compare Fig. 7(b). For a quantitative determination of mullite, α-$Al_2O_3$, and silicon carbide as crystalline phases relative to each other, Rietveld refinement of the experimental diffraction pattern was used (Table 2).

The elemental analyses of the ceramic samples annealed at 1500 °C (Table 3) show that the carbon content in the aluminum modified silicon oxycarbide materials was found to be lower than that of MK-derived SiOC ceramic (14.80%).[28] Nevertheless, the calculated "free" carbon content (according to the scheme reported by Harshe[46]) in SiAlOC samples was found to be remarkably lower (<1 wt.%) than in that of SiOC ceramics (11 wt.%). Thus, although the aluminum derivate SiOC ceramics generate a significant decrease of the total carbon content, the effect of aluminum filler is visible towards decreasing the amount of the "free" carbon in the ceramic matrix. Moreover, a good agreement between the results obtained from the elemental analysis and the Rietveld analysis is achieved.

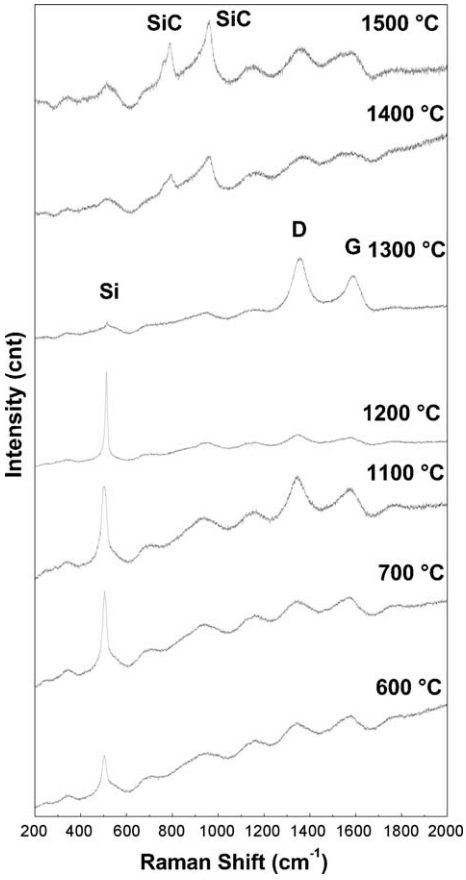


Fig. 3. Representative micro-Raman spectra of the sample AlMK.

The micro-Raman spectra recorded in the region 200–2000 $cm^{-1}$ for the pyrolyzed and annealed AlMK ceramic samples are depicted in Fig. 3. The samples pyrolyzed at temperatures of 1100, 1200 and 1300 °C are characterized by an intrinsic fluorescence which hinders the acquisition of qualitatively appropriate spectra. Nevertheless, the samples clearly exhibit one absorption band located in the region of 524 $cm^{-1}$ which is characteristic for free silicon. Annealing at 1400 and 1500 °C induces structural changes in the ceramic matrix observable by the recorded micro-Raman spectra. Two

Table 3
Elemental analyses, empirical formula and theoretical weight percentage of the phases calculated for the AlMK sample.

| Material | Composition (wt.%) | | | | Empirical formula | $Al_2O_3$ | $SiO_2$ | Mullite | SiC | $C_{free}$ |
|---|---|---|---|---|---|---|---|---|---|---|
| | Si | Al | O | C | | | | | | |
| AlMK/1500 °C | 31.42 | 25.93 | 31.92 | 10.73 | $SiAl_{0.86}O_{1.78}C_{0.80}$ | 6.67 | – | 58.97 | 33.75 | 0.64 |

strong absorption bands for the AlMK sample annealed at 1400 °C located in the region of 1350 $cm^{-1}$ and 1582 $cm^{-1}$ are characteristic for the so called G- and D-bands[47–49] and illustrate the formation of free disordered graphitic carbon. At 1500 °C the relative intensity of these bands seems to decrease and in the region 750–1000 $cm^{-1}$ characteristic absorption bands of cubic β-SiC polymorph (3C–SiC) marked by peaks around 799 and 974 $cm^{-1}$ are observed.[50–52] Silicon carbide crystallites may be present in the ceramic matrix well before their Raman spectral fingerprint is observed (XRD pattern proofed the presence of SiC starting with 800 °C), because, due to their optical absorption, the Raman scattering efficiency of carbon species (e.g. graphite) can be assumed to be at least ten times higher than that of SiC.[50] These results indicate that after annealing at 1500 °C carbon is found to be enclosed in the ceramic matrix in the form of a $sp^2$-hybridized carbon network in a low crystalline state. Although the X-ray diffraction measurements clearly showed the presence of mullite in ceramic samples above 1300 °C, however, the alumosilicate $3Al_2O_3 \times 2SiO_2$ could not be detected by micro-Raman spectroscopy.

The ceramization process of the AlMK sample as well as the ceramic samples obtained after pyrolysis and after annealing was also investigated by FT-IR spectroscopy with the measured spectra depicted in Fig. 4. The spectra of the as received MK polysiloxane is also shown for direct comparison and found similar to earlier reported data.[28,29,46] The infrared spectroscopic transition wavenumbers and assignments for all the samples are given in Table 4. The FT-IR analysis of the MK polymer leads to the classification of various bands and support the structure proposal of the MK polymer.[28,29,46] Relevant changes in the FT-IR spectra of the AlMK samples are observed and the band assignments agree with the results of the XRD and Raman spectra. Up to 800 °C the absorption bands of Si–$CH_3$ and C–H bonds (1276 $cm^{-1}$, 2974 $cm^{-1}$, and 2913 $cm^{-1}$) slowly disappear suggesting the cleavage of the Si–$CH_3$ bonds and their replacement with Si–O–Si bonds indicating the formation of a ceramic network. The bands at 576 $cm^{-1}$ (Si–O) and 549 $cm^{-1}$ (Si–C) disappear at 700 °C. Further assignment of the bands localized in the low frequency region of IR spectrum (<1200 $cm^{-1}$) for the heat treated AlMK samples become difficult as the $Al_4C_3$, $Al_2O_3$, SiC and mullite phases, characterized by the other spectroscopic methods (XRD, Raman), exhibit broad features which broadly overlap in this spectral region.[53–61] Nevertheless, the Al–C stretch and in carbides (as in $Al_4C_3$) is observed near 760 $cm^{-1}$ (see Table 4) up to 1000 °C,[58] the bands located around the frequencies of 580 and 445 $cm^{-1}$ are characteristic for the Al-O bonding in $Al_2O_3$.[53–57] SiC shows strong absorption at or near 800 $cm^{-1}$ above 900 °C; the measured IR spectrum of the AlMK sample annealed above 1300 °C resembles that of the mullite phase which shows a number of broad bands and shoulders. In the region 1125–1165 $cm^{-1}$ the Si–O stretching frequencies are identified, as well as the band at 730 $cm^{-1}$ as a tetrahedral (Al or Si) bend and the band at 580 $cm^{-1}$ as an octahedral Al–O stretch.[59–61]

Table 5 illustrates the bulk and Archimedes density respectively. The open porosity values for the ceramic samples

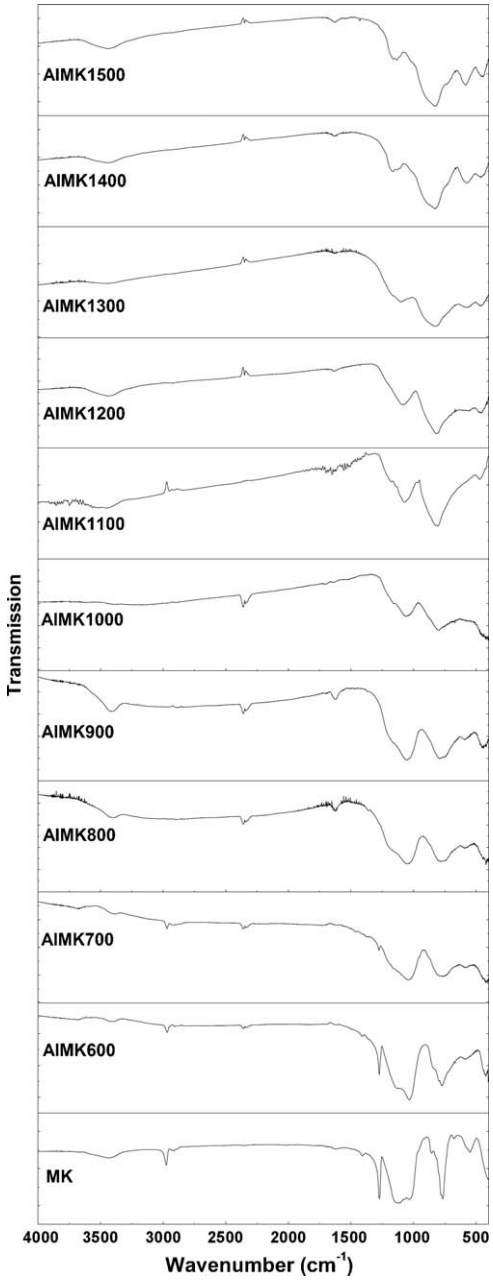


Fig. 4. Representative IR spectra of the sample AlMK.

pyrolyzed at 1300 °C and annealed at 1400 and 1500 °C are also shown. The open porosity and the densities increase with the annealing temperature; the sample AlMK exhibits a relatively high open porosity of ~27% at 1500 °C.

SEM and TEM studies completed our investigations. The SEM micrographs shown in Fig. 5 represent bulk samples of the mixtures warm-pressed and annealed in argon at 1300 and 1500 °C. The ceramic samples illustrate that the residual porosity has a rather homogeneous dispersion in the bulk material. No new information regarding the microstructure of the ceramics could be extracted from the SEM images taken with high magnification in the pore areas, therefore, the sample AlMK annealed at 1500 °C was also investigated by means of TEM and HRTEM as shown in Figs. 6 and 7. The presence of 3/2

Table 4
Observed IR bands and possible assignments for the samples studied here (wavenumbers).

| MK | AlMK | | | | | | | | | | Assignments |
|---|---|---|---|---|---|---|---|---|---|---|---|
| | 600 °C | 700 °C | 800 °C | 900 °C | 1000 °C | 1100 °C | 1200 °C | 1300 °C | 1400 °C | 1500 °C | |
| 2974 m | 2969 m | 2969 w | | | | | | | | | $\nu_{as}$(–$CH_3$) |
| 2913 w | 2908 w | 2918 vw | | | | | | | | | $\nu_s$(–$CH_3$) |
| 1273 s | 1275 s | 1276 m | | | | | | | | | $\delta$ C–H (Si–$CH_3$) |
| | | | 1164 sh | 1164 sh | 1164 sh | 1174 sh | 1174 sh | 1174 sh | 1165 s | 1165 s | $\nu_{as}$(Si–O–Si) of $SiO_4$ |
| 1130 s | 1134 sh | 1128 sh | | | | | | | | | $\nu_{as}$(Si–O–Si) |
| | | | | | | 1075 s | 1085 s | 1103 s | 1130 s | 1130 s | $\nu_{as}$(Si–O–Al) |
| 1074 s | | | | | | | | | | | $\nu_a$(Si–O–Si) |
| 1035 s | 1035 s | 1035 s | 1050 s | 1050 s | 1050 s | 1030 sh | | | | | $\nu_a$(Si–O–Si) |
| 857 w | 845 sh | | | | | | | | | | D(Q) ($SiO_2C_2$) |
| | | | | 792 s | 800 s | 807 s | 815 s | 828 s | 831 s | 828 s | $\nu$(Si–C) (ceramic) |
| 783 sh | 797 sh | 775 s br | 775 s | | | | | | | | $\nu_a$(Si–O) |
| 767 s | 772 s | 745 sh | 745 sh | 750 sh | | | | | | | $\nu_a$(Si–C) |
| | | | | | | | | 730 sh | 730 sh | 730 sh | $\nu$ (O–Al–O)/$\nu$ (Al–O) |
| 575 sh | | | | | | | | | | | $\nu$(Si–O) |
| | 586 m | 582 m br | 580 m br | 587 m br | | | 565 m | 576 m | 570 m | 582 m | $\nu$ (Al–O) ($Al_2O_3$) |
| 549 m | | | | | | | | | | | $\nu$(Si–C) |
| | | | | 451 m | | 474 m | 460 m | 465 m | 462 m | 446 m | $\nu$ (Al–O) ($Al_2O_3$) |

The notations: s, strong; m, medium; w, weak; vw, very weak; sh, shoulder; br, broad.

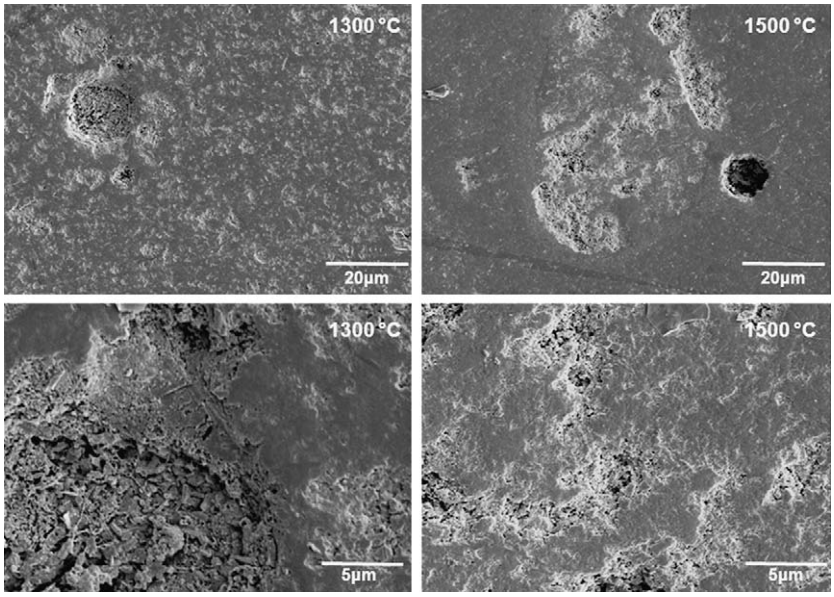


Fig. 5. Scanning electron microscope micrographs of the surface morphology of selected samples after heat treatment at 1300 and 1500 °C. Magnifications of 1000× and 10,000× were used for taking the pictures.

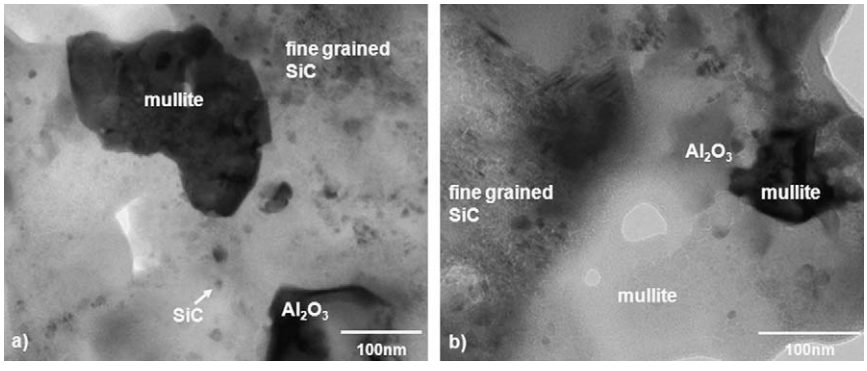


Fig. 6. TEM bright field images of the microstructure of material AlMK, annealed at 1500 °C. Regions of mullite, alumina and fine grained SiC precipitations are adjacent to each other. It should be noted that the dispersion of the individual phases is not homogenous in this sample.

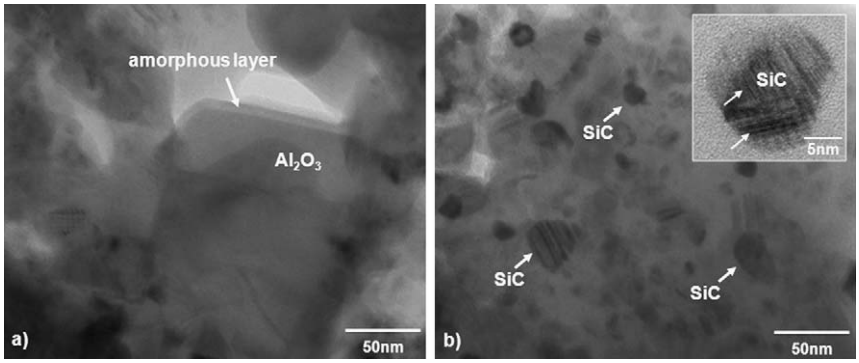


Fig. 7. TEM bright field images (a) of a residual alumina grain covered by a thin amorphous layer. This microstructural feature indicated that the mullitization process is not completed yet, even upon annealing at 1500 °C. (b) An area with a high volume fraction of silicon carbide precipitates. The HRTEM image (inset) reveals the presence of stacking faults and microtwins, typical for β-SiC.

mullite matrix grains with a crystallite size up to 200 nm was confirmed by bright field imaging. Figs. 6 and 7 depict overviews of the microstructure where mullite, alumina and fine grained SiC precipitates are adjacent to each other. It should be noted that all particle sizes determined by TEM are slightly higher than those obtained by XRD analysis, which could be the result not only of residual stress within the sample but also by possible lattice disorders. The HRTEM image (inset in Fig. 7(b)) clearly reveals stacking faults and microtwins, typical for β-SiC, being consistent with XRD-Rietveld refinement analysis. It should be noted that the dispersion of the nanosized SiC precipitates is not homogenous in this sample. Areas with a high volume fraction of SiC adjacent to regions with hardly any SiC formation were often found (compare also Fig. 6(b)). The origin of this inhomogeneity is thought to be a consequence of the phase separation of SiOC to $SiO_2$ and SiC. The separated $SiO_2$ will be converted to mullite by the reaction with $Al_2O_3$ leading to the above mentioned phenomenon of an inhomogeneous distribution of SiC. The formation and decomposition of the aluminum carbide phase during pyrolysis with subsequent formation of silicon carbide in addition influence the microstructural development of the ceramic matrix.

The sample AlMK shows the onset of mullite formation at temperatures between 1200 and 1300 °C; enhanced mullitization is observed after the annealing steps at 1400 and 1500 °C. The detection of a thin glassy layer on the surface of individual alumina grains, as observed by TEM (Fig. 7(a)), indicates that the mullitization process is not completed. A further increasing in the annealing temperature and/or annealing time might lead to full transformation. Nevertheless, the low mullite formation temperature is strongly connected with the composition of the starting polymer/filler mixture, namely aluminum filler with a particle size in the nanometric range and the MK polysiloxane polymer. The possible reaction mechanism for mullite formation at low temperatures involve in first a reaction step of Al with the SiOC preceramic matrix to give transient γ-$Al_2O_3$, followed by the reaction with silica to form mullite nuclei and additionally conversion to α-$Al_2O_3$. A solid-state reaction between amorphous $SiO_2$ and $Al_2O_3$ leads also to the formation of a mullite phase.[62–64] The increased reactivity of the Al filler towards the SiOC matrix is supposed to be influenced also by the size of the filler particles which additionally enhances the homogeneity of the starting mixtures. Therefore, an enhanced segregation of a silicon carbide phase is observed starting already at the pyrolysis temperature of about 800 °C. Crystallite sizes around 10 nm for the silicon carbide phase were found with a fairly homogenous distribution in the ceramic matrix. Silicon carbide segregation at such low temperatures is closely related to three facts: the depletion of oxygen in the SiOC matrix by Al, the presence of carbon atoms in the neighborhood of silicon atoms in the MK polymer skeleton and the decomposition reaction of $Al_4C_3$. Development of free Si is also found during the ceramization process, and is caused by the reaction of Al with the SiOC matrix and SiC respectively. As a side reaction we note here the formation of an unintentional $Al_4C_3$ phase, an unstable product which decomposes upon increase of the pyrolysis temperature.

Table 5
Density and porosity values of the samples prepared.

| Sample | $\rho_{bulk}$ (g/cm$^3$) | $\rho_{arch}$ (g/cm$^3$) | Open porosity (%) |
|---|---|---|---|
| AlMK | | | |
| 1300 °C | 2.16 | 2.82 | 23.26 |
| 1400 °C | 2.19 | 2.88 | 23.95 |
| 1500 °C | 2.31 | 3.14 | 26.35 |

## 4. Conclusions

Modification of the polysiloxane MK polymer with nano-aluminum following the principles of the active-filler pyrolysis results in the formation of a SiC–mullite–$Al_2O_3$-based ceramic nanocomposite at temperatures around 1500 °C. The composite is characterized by particle sizes which do not exceed 20 nm for SiC, 200 nm for mullite and 50 nm for α-$Al_2O_3$ respectively.

Due to the high reactivity of the nano-aluminum filler particles with silica, formed upon phase separation of SiOC, mullite starts to crystallize at unusually low temperatures (about 1300 °C). Moreover, segregation of a silicon carbide phase also starts at very low temperatures (800 °C) and α-$Al_2O_3$ was detected at temperatures of about 1300 °C. Hence, such a high temperature stable nanocomposite can be processed at rather low temperatures e.g., at 1300 °C, since no major grain coars-

ening and phase transitions were observed upon annealing at 1500 °C.

## Acknowledgments

The work reported here is part of the Priority Program "Nanoscaled Inorganic Materials by Molecular Design: New Materials for Advanced Technologies" (DFG-SPP 1181) funded by the Deutsche Forschungsgemeinschaft, Bonn, Germany. R.R. also thanks the Fonds der Chemischen Industrie, Frankfurt, Germany, for financial support.

## References

1. Sternitzke M. Review: structural ceramic nanocomposites. *J Eur Ceram Soc* 1997;**17**:1061–82.
2. Andres RP, Averback RS, Brown WL, Bras LE, Goddard WA, Kaldor A, et al. Research opportunities on clusters and cluster-assembled materials—a Department of Energy, Council on Materials Science Panel Report. *J Mater Res* 1989;**4**:704–36.
3. Siegel RW, Ramasamy S, Hahn H, Li Z, Lu T, Gronsky R. Synthesis, characterization, and properties of nanophase $TiO_2$. *J Mater Res* 1988;**3**:1367–72.
4. Niihara K. New design concept of structural ceramics–ceramic nanocomposites. *J Ceram Soc Jpn* 1991;**99**:974–82.
5. Erny T, Seibold M, Jarchow O, Greil P. Microstructure development of oxycarbide composites during active-filler-controlled polymer pyrolysis. *J Am Ceram Soc* 1993;**76**:207–13.
6. Greil P. Active-filler-controlled pyrolysis of preceramic polymers. *J Am Ceram Soc* 1995;**78**:835–48.
7. Greil P. Near net shape manufacturing of polymer derived ceramics. *J Eur Ceram Soc* 1998;**18**:1905–14.
8. Greil P. Polymer derived engineering ceramics. *Adv Eng Mater* 2000;**2**:339–48.
9. Renlund GM, Prochazka S, Doremus RH. Silicon oxycarbide glasses. Part I. Preparation and chemistry. *J Mater Res* 1991;**6**:2716–22.
10. Renlund GM, Prochazka S, Doremus RH. Silicon oxycarbide glasses. Part II. Structure and properties. *J Mater Res* 1991;**6**:2723–34.
11. Marple BR, Green DJ. Mullite/alumina particulate composites by infiltration processing. III. Mechanical properties. *J Am Ceram Soc* 1991;**74**:2453–9.
12. Gao L, Jin X, Kawaoka H, Sekino T, Niihara K. Microstructure and mechanical properties of SiC–mullite nanocomposite prepared by spark plasma sintering. *Mater Sci Eng* 2002;**A334**:262–6.
13. Ando K, Furusawa K, Chu MC, Hanagata T, Tuji K, Sato S. Crack-healing behavior under stress of mullite/silicon carbide ceramics and the resultant fatigue strength. *J Am Ceram Soc* 2001;**84**:2073–8.
14. Takahashi K, Uchiide K, Kimura Y, Nakao W, Ando K, Yokouchi M. Threshold stress for crack healing of mullite reinforced by SiC whiskers and SiC particles and resultant fatigue strength at the healing temperature. *J Am Ceram Soc* 2007;**90**:2159–64.
15. Andoa K, Chua M-C, Tsujib K, Hirasawac T, Kobayashid Y, Satod S. Crack healing behavior and high-temperature strength of mullite/SiC composite ceramics. *J Eur Ceram Soc* 2002;**22**:1313–9.
16. Soraru GD, Kleebe H-J, Ceccato R, Pederiva L. Development of mullite–SiC nanocomposites by pyrolysis of filled polymethylsiloxane gels. *J Eur Ceram Soc* 2000;**20**:2509–17.
17. Suttor D, Kleebe H-J, Ziegler G. Formation of mullite from filled siloxanes. *J Am Ceram Soc* 1997;**80**:2541–8.
18. Anggono J, Derby B. Intermediate phases in mullite synthesis via aluminum- and alumina-filled polymethylsiloxane. *J Am Ceram Soc* 2005;**88**:2085–91.
19. Michalet T, Parlier M, Beclin F, Duclos R, Crampon J. Elaboration of low shrinkage mullite by active filler controlled pyrolysis of siloxane. *J Eur Ceram Soc* 2002;**22**:143–52.
20. Anggono J, Derby B. Mullite formation from the pyrolysis of aluminum-loaded polymethylsiloxanes: the influence of aluminum powder characteristics. *J Eur Ceram Soc* 2006;**26**:1107–19.
21. Colombo P, Riccardi B, Donato A, Scarinci G. Joining of SiC/$SiC_f$ ceramic matrix composites for fusion reactor blanket applications. *J Nucl Mater* 2000;**278**:127–35.
22. Narisawa M, Kado H, Mabuchi H, Kim Y-W. Accelerated ceramization of polymethylsilsesquioxane by aluminum-based filler reductant. *Appl Organom Chem* 2010;**24**:612–7.
23. Riedel R, Toma L, Fasel C, Miehe G. Polymer-derived mullite–SiC-based nanocomposites. *J Eur Ceram Soc* 2009;**29**:3079–90.
24. http://www.ill.eu/sites/fullprof/index.html.
25. Kawamura T. Silicon carbide crystals grown in nitrogen atmosphere. *Mineral J (Japan)* 1965;**4**:333–55.
26. Balzar D, Ledbetter H. Crystal structure and compressibility of 3-2 mullite. *Am Miner* 1993;**78**:1192–6.
27. Brown AS, Spackman MA, Hill RJ. The electron distribution in corundum. A study of the utility of merging single-crystal and powder diffraction data. *Acta Cryst* 1993;**A49**:513–27.
28. Harshe R, Balan C, Riedel R. Amorphous Si(Al)OC ceramic from polysiloxanes: bulk ceramic processing, crystallization behavior and applications. *J Eur Ceram Soc* 2004;**24**:3471–82.
29. Ionescu E, Linck C, Fasel C, Müller M, Kleebe H-J, Riedel R. Polymer-derived SiOC/$ZrO_2$ ceramic nanocomposites with excellent high-temperature stability. *J Am Ceram Soc* 2010;**93**:241–50.
30. Wu S, Holz D, Claussen N. Mechanisms and kinetics of reaction-bonded aluminum oxide ceramics. *J Am Ceram Soc* 1993;**76**:970–80.
31. Li D, Hwang ST. Pyrolysis kinetics of highly crosslinked polymethylsiloxane by TGA. *J Appl Polym Sci* 1992;**44**:1979–91.
32. Jeffrey GA, Wu V. The structure of the aluminum carbonitrides. II. *Acta Cryst* 1966;**A20**:538–47.
33. Chase Jr MW. NIST-JANAF thermochemical tables, fourth edition. *J Phys Chem Ref Data Monograph* 1998;**9**:1–1951.
34. Scott VD, Chen AS. Collected studies on interfaces and interphases as related to the behavior of fibre-reinforced aluminum alloy composites. *J Microsc* 1999;**196**:86–102.
35. Laurent V, Chatain D, Eustathopoulos N. Wettability of SiC by aluminum and Al–Si alloys. *J Mater Sci* 1987;**22**:244–50.
36. Noble B, Trowsdale AJ, Harris SJ. Low-temperature interface reaction in aluminium–silicon carbide particulate composites produced by mechanical alloying. *J Mater Sci* 1997;**32**:5969–78.
37. Viala JC, Fortier P, Bouix J. Stable and metastable phase equilibria in the chemical interaction between aluminium and silicon carbide. *J Mater Sci* 1990;**25**:1842–50.
38. Iseki T, Kameda T, Maruyama T. Interfacial reactions between SiC and aluminium during joining. *J Mater Sci* 1984;**19**:1692–8.
39. Saito Y, Takei T, Hayashi S, Yasumori A, Okada K. Effects of amorphous and crystalline $SiO_2$ additives on γ-$Al_2O_3$-to-α-$Al_2O_3$ phase transitions. *J Am Ceram Soc* 1998;**81**:2197–200.
40. Scherrer P. Bestimmung der Größe und der inneren Struktur von Kolloidteilchen mittels Röntgenstrahlen. *Nachr Ges Wiss Gottingen Math-Phys Kl* 1918;**2**:98–100.
41. Karen P, Woodward PM. Liquid-mix disorder in crystalline solids: $ScMnO_3$. *J Solid State Chem* 1998;**141**:78–88.
42. Pujar VV, Cawley JD. Effect of stacking faults on the X-ray diffraction profiles of β-SiC powders. *J Am Ceram Soc* 1995;**78**:774–82.
43. Pujar VV, Cawley JD. Computer simulations of diffraction effects due to stacking faults in β-SiC. I. Simulation results. *J Am Ceram Soc* 1997;**80**:1653–62.
44. Pujar VV, Cawley JD. Microstructural evolution in liquid-phase-sintered SiC. Part I. Effect of starting powder. *J Am Ceram Soc* 2001;**84**:1578–84.
45. Pujar VV, Cawley JD. Computer simulation of diffraction effects due to stacking faults in β-SiC. II. Experimental verification. *J Am Ceram Soc* 2001;**84**:2645–51.
46. Harshe RR. Synthesis and processing of amorphous Si(Al)OC bulk ceramics: high temperature properties and applications. *Ph.D. Thesis, TU Darmstadt, FB Material- und Geowissenschaften* 2004.

47. Ferrari AC, Robertson J. Interpretation of Raman spectra of disordered and amorphous carbon. *Phys Rev B* 2000;**61**:14095–107.
48. Pimenta MA, Dresselhaus G, Dresselhaus MS, Cancado LG, Jorio A, Saito R. Studying disorder in graphite-based systems by Raman spectroscopy. *Phys Chem Chem Phys* 2007;**9**:1276–91.
49. Ferrari AC, Meyer JC, Scardaci V, Casiraghi C, Lazzeri M, Mauri F, et al. Raman spectrum of graphene and graphene layers. *Phys Rev Lett* 2006;**97**:187401–4.
50. Sasaki Y, Nishina Y, Sato M, Okamura K. Raman study of SiC fibres made from polycarbosilane. *J Mater Sci* 1987;**22**:443–8.
51. Gouadec G, Colomban P. Non-destructive mechanical characterization of SiC fibers by Raman spectroscopy. *J Eur Ceram Soc* 2001;**21**:1249–59.
52. Ward Y, Young RJ, Shatwell RA. Application of Raman microscopy to the analysis of silicon carbide monofilaments. *J Mater Sci* 2004;**39**:6781–90.
53. Alexandrescu R, Borsella E, Botti S, Cesile MP, Martelli S, Giorgi R, et al. Synthesis of aluminum oxide-based ceramics by laser photo-induced reactions from gaseous precursors. *J Mater Res* 1997;**12**:774–82.
54. Katamreddy R, Inman R, Jursich G, Soulet A, Nicholls A, Takoudis C. Post deposition annealing of aluminum oxide deposited by atomic layer deposition using tris(diethylamino)aluminum and water vapor on Si(1 0 0). *Thin Solid Films* 2007;**515**:6931–7.
55. Baraton MI, Quintard P. Infrared evidence of order–disorder phase transition ($\gamma \rightarrow \delta \rightarrow \alpha$) in $Al_2O_3$. *J Mol Struct* 1982;**79**:337–40.
56. Chowdhuri AR, Takoudis CG. Investigation of the aluminum oxide/Si(1 0 0) interface formed by chemical vapor deposition. *Thin Solid Films* 2004;**446**:155–9.
57. Shek CH, Lai JKL, Gum TS, Lin GM. Transformation evolution and infrared absorption spectra of amorphous and crystalline nano-$Al_2O_3$ powders. *Nano Struct Mater* 1997;**8**:605–10.
58. Fondeur F, Mitchell BS. Fourier transform infrared studies of propane pyrolysis over calcium aluminate melts. *J Am Ceram Soc* 1998;**81**:1045–9.
59. MacKenzie KJD. Spectroscopy of mullite and compounds with mullite-related structures. In: Schneider H, Komarneni S, editors. *Mullite*. Weinheim: Wiley-VCH; 2005. p. 18926.
60. Padmaja P, Anilkumar GM, Mukundan P, Aruldhas G, Warrier KGK. Characterisation of stoichiometric sol–gel mullite by Fourier transform infrared spectroscopy. *Int J Inorg Mater* 2001;**3**:693–8.
61. Percival HJ, Duncan JF, Foster PK. Interpretation of the kaolinite–mullite reaction sequence from infrared absorption spectra. *J Am Ceram Soc* 1974;**57**:57–61.
62. Saruhan B, Albers W, Kaysser WA. Reaction and sintering mechanisms of mullite in the systems cristobalite/$\alpha$-$Al_2O_3$ and amorphous $SiO_2$/$\alpha$-$Al_2O_3$. *J Eur Ceram Soc* 1996;**16**:1075–81.
63. Kleebe H-J, Hilz G, Ziegler G. TEM and EELS characterization of the glass phase in sol–gel derived mullite. *J Am Ceram Soc* 1996;**79**:2592–600.
64. Kleebe H-J, Siegelin F, Staubinger T, Ziegler G. Conversion of $Al_2O_3$–$SiO_2$ powder mixtures to 3:2 mullite following the stable or metastable phase diagram. *J Eur Ceram Soc* 2001;**21**:2521–33.